

Article

Probabilistic-Based Assessment of Liquefaction-Induced Damage with Analytical Fragility Curves

Davide Forcellini 

Civil and Environmental Engineering, University of Auckland, 20 Symonds Street, Auckland 1010, New Zealand; dfor295@aucklanduni.ac.nz

Received: 21 July 2020; Accepted: 13 August 2020; Published: 15 August 2020



Abstract: Soil liquefaction may cause severe damages to structures mainly in terms of lateral spread and settlements, as documented during historical earthquakes. Liquefaction-potential (LP) estimation has become an important issue in seismic assessment, and this paper aims to propose a new methodology based on fragility curves. LP curves were developed and applied to two case studies performed with 3D numerical models applying Opensees. Nonlinear hysteretic materials and advanced plasticity models were used to reproduce the high nonlinear mechanisms of liquefaction, such as strong dilation tendency and cyclic shear behaviour. LP curves were applied to compare the results of the performed free field (FF) and soil–structure interaction (SSI) case studies.

Keywords: liquefaction-potential (LP) curves; new methodology; liquefaction risk; numerical simulations; Opensees

1. Introduction

Historical earthquakes (Niigata, Japan 1964, Dagupan City, Philippines 1990, Chi-Chi, Taiwan 1999, Japan 2011, Kocaeli, Turkey 1999 and Christchurch, New Zealand, 2011) demonstrated the importance of estimating liquefaction-induced damages, mainly in terms of permanent lateral spread and settlements. In this regard, liquefaction potential assessment has been based on empirical data (e.g., [1–4]) and many relationships between liquefaction resistance and soil parameters have been proposed [5–15]. Among them, Halder, A. [7] applied SPT results to a second-moment statistical analysis as a development of the empirical procedure introduced by Robertson, P.K [12]. In the Italian background, Crespellani, T. [16–18] proposed several approaches for the assessment of liquefaction potential. In this regard, Di Ludovico, M. [19] developed empirical fragility curves to analyse liquefaction-induced effects during the 2012 Emilia Romagna earthquake. Moreover, Kafali, C. [20] estimated the probability of liquefaction as a function of earthquake load and SPT resistance by logistic regression analyses, while other researchers proposed an advanced first-order second-moment (AFOSM) technique to calculate the probability of failure, [9]. Juang, C.H. [8] performed an extensive series of sensitivity analyses using the first-order reliability method associated with mapping functions to characterise the uncertainties in the performance function.

However, as pointed out by Juang, C.H. [8], such methodologies aimed to assess ground and foundation deformation but rarely to determine liquefaction effects on existing structures and the subsequent liquefaction-induced structural damages. In this regard, the determination of liquefaction potential has become a fundamental issue in the assessment of the induced damage to civil engineering structures by applying several methodologies. A class of approaches was based on the use of artificial neural networks (ANN) models [21–26] that may estimate the relationships between the soil and earthquake characteristics with the liquefaction potential, requiring no prior knowledge of the form of

the relationships. However, the main disadvantage of such approaches consists of the deterministic definition of soil parameters that cannot consider many uncertainties. Recently, the development of numerical simulations of nonlinear dynamic soil–structure–interaction (SSI) analyses provided probabilistic-based insights into the liquefaction-induced effects (e.g., [27–38]).

Furthermore, damage prediction is essential for the assessment of economic losses, and fragility curves are interesting representations of its cumulative distribution, providing helpful information on the probability that specific levels of damage have risen or exceeded. Fragility curves have been applied to estimate structural damages due to ground shaking (e.g., [39,40]) as a way of expressing the probability of exceeding specific limit states. In this regard, probabilistic-based approaches based on analytical fragility curves are widely developed in the literature for structures and infrastructures [41–46]. Recently, Liang, H. [47] proposed one of the most recent applications of fragility curves to study the seismic vulnerability of a high concrete arch dam based on seismic instability and taking the friction coefficients and cohesions as random parameters. In another contribution, Caverzan, A. [41] applied analytical fragility curves to study the influence of dynamic SSI effects on the assessment of the seismic vulnerability of buildings. In particular, Shinozuka, M. [48] developed a statistical procedure for reliability analyses by applying two-parameter lognormal distribution functions to develop empirical and analytical fragility curves for bridges. The Monte Carlo approach was also applied by Kafali, C. and Hwang, H.M. [20,49].

Fragility curves may include many sources of uncertainties, such as the ones connected with the soil characterisations and properties. For example, Hwang, H.M. [49] considered uncertainties, such as viscous damping ratio, strength and stiffness of structural materials, Shinozuka, M. [48] included variability in ground motions, and Popescu, R. [50] developed fragility curves that account for the variability of soil properties during liquefaction. In this regard, the study of liquefaction effects on structural fragility curves was the object of several contributions, such as Aygün, B. [51] who performed a coupled 3D bridge–foundation system with 2D heterogeneous soil strata finite element (FE) models to monitor multiple bridge failure mechanisms in the presence of 1D soil site amplifications and liquefaction effects. Recently, Fotopoulou, S. [52] presented a numerical framework for the vulnerability assessment of low-code Masonry Reinforced Concrete (MRF RC) buildings subjected to liquefaction-induced differential displacements.

In the previous contributions, fragility curves were used to include liquefaction to demonstrate its role in the assessment of structural vulnerability. The novelty of the presented study instead consists of proposing the application of fragility curves to estimate liquefaction potential and applying it to two case studies. Analytical fragility curves are here developed to estimate the probability of liquefaction in terms of lateral spread and settlement with 3D numerical models, first for free field (FF) conditions, and then considering SSI effects.

2. Liquefaction-Potential Curves

The fragility curve has been proposed as a well-established approach in earthquake engineering to consider uncertainties in demand and capacity. They represent graphical relationships between the conditional probability of exceeding predefined damage states (DS) for given levels of EDP (engineering demand parameters) and are used to estimate the amount of damage for a particular level of shaking defined with intensity measures (IM). For example, fragility curves, based on HAZUS-MH MR5: Technical Manual [43], consist of considering four states (slight, moderate, extensive, complete), and they display the probability that the response of a system exceeds a given threshold limit given a certain excitation level, as applied in Ranjbar, P.R.'s work [46]. Lateral spread displacements and settlement at the surface were chosen as EDPs to assess the seismic effects of liquefaction on FF and SSI systems and thus developing analytical fragility curves to define liquefaction-induced damage. Peak Ground Acceleration (PGA) is selected as the IM, scaled to multiple levels from zero to 1.0 g with steps of 0.1 g, following the well-credited approach of incremental dynamic analysis (IDA) proposed by Hwang, H.M. [49]. Thus, a number of 10×7 IDA nonlinear analyses were performed (with Opensees

PL) for each case study (total 140). The input motions (Figure 1 and Table 1) were selected from the Pacific Earthquake Engineering Research (PEER) Center Next generation Attenuation (NGA) database (<http://peer.berkeley.edu/nga/>), ([53,54] on the base of Eurocode prescriptions) to significantly affect the dynamic characteristics of the system and was applied at the base of the models, along the x-axis (longitudinal direction). In particular, IDA requires a series of nonlinear, dynamic time history analyses for the selected ensemble of ground motions with increasing intensity levels to cover the entire range of the response, from elastic behaviour through liquefaction condition. Therefore, the limit state was chosen as the liquefaction condition ($r_u = 1$). Pore pressure ratio (r_u), defined previously in [5], considers the pore pressure as a fraction of the vertical stress (including the weight of ponded water, if the material is submerged) [32]. This study assumes that all uncertainties in the fragility curves can be represented by lognormal distributions, and, thus, only two parameters were needed to plot the curves, the logarithmic mean (μ) and standard deviation (β) of the lognormal seismic intensity measure (PGA). In particular, there are several reasons that justify the use of lognormal distribution: (1) its simplicity in approximating an uncertainty quantity that must take on a positive value, using only an estimate of the central value and uncertainty, (2) the fact that it has been widely used for several decades in earthquake engineering and (3) it is the distribution that assumes the least knowledge (the only variables are the mean and logarithmic standard deviation). Therefore, IDA analysis results were represented to build linear regression and define the mean and log-standard deviation values. Moreover, the probability of liquefaction ($r_u = 1$) for a specific intensity (PGA) was then calculated as

$$P[r_u = 1|PGA] = \phi\left(\frac{\ln(PGA) - \mu}{\beta}\right) \quad (1)$$

where ϕ is the standard normal cumulative distribution function.

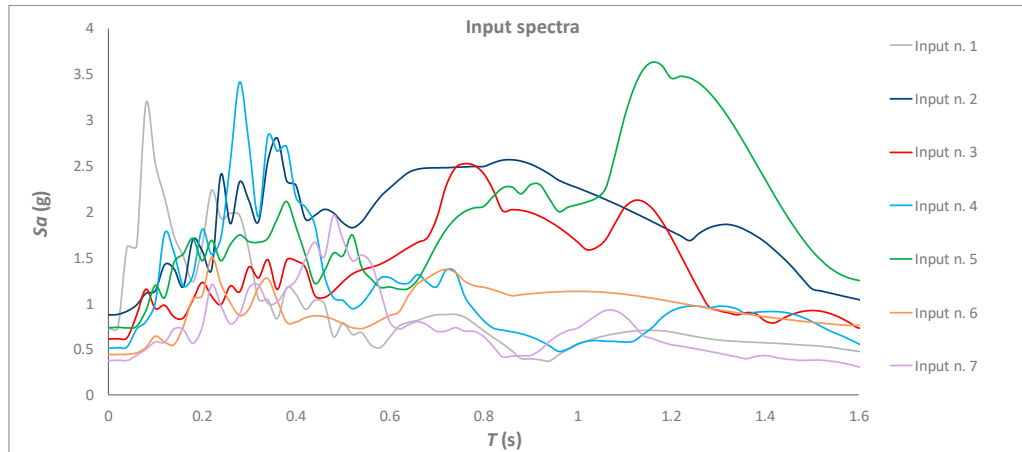


Figure 1. Selected input motions.

Table 1. Input motions characteristics: Peak Ground Acceleration (PGA), Peak Ground Velocity (PGV), Peak Ground Displacement (PGD).

Input Motion	Station	PGA(g)	PGV (cm/s)	PGD (cm)
n.1 Landers (1992)	Lucerne Valley	0.72	147.45	265.14
n.2 Northridge (1994)	Rinaldi Receiving	0.89	185.08	60.07
n.3 Northridge (1994)	Sylmar Converter	0.70	135.82	58.20
n.4 Northridge (1994)	Sylmar Hospital	0.87	139.54	50.37
n.5 Hyogo-ken (1995)	Takatori	0.74	155.44	44.95
n.6 Erzincan (1992)	Erzincan	0.44	125.80	53.30
n.7 El Centro (1940)	Calthech Ha001	0.35	38.47	82.44

3. Finite Elements Models

Finite element models were performed by OpenSeesPL [23,35], from the Pacific Earthquake Engineering Research (PEER) Center. 3D finite models were developed to capture many outputs (e.g., the mechanism of excess pore pressure, accelerations, displacements, settlements, tilts, and inter-story drifts) that are otherwise impossible to be assessed with 1D numerical simulations. The study here proposed was divided into two steps (Table 2), while 3D numerical models are shown in Figures 2 and 3.

Table 2. Numerical analyses.

Numerical Analyses	Mesh	Type
Step 1	Figure 2	Free field (FF)
Step 2	Figure 3	Soil–structure interaction (SSI)

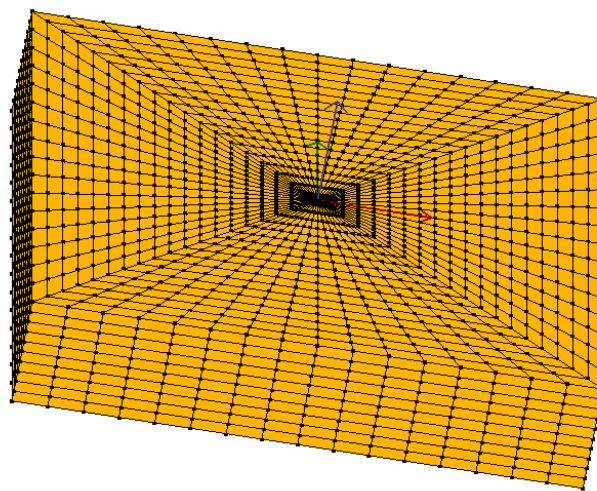


Figure 2. Step 1: 3D Numerical model. Free field analysis.

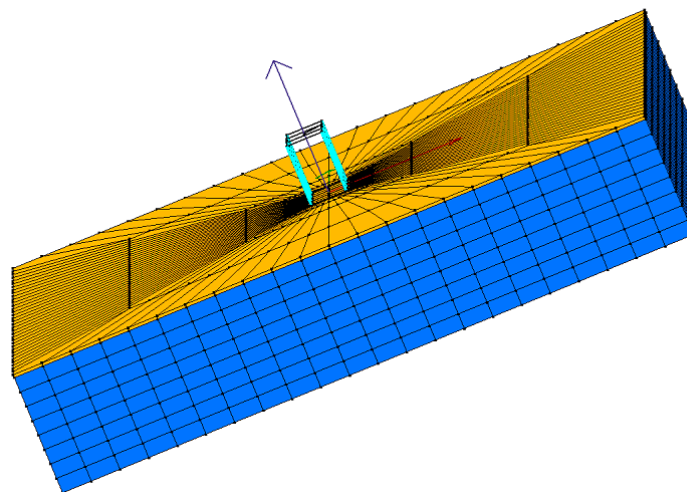


Figure 3. Step 2: 3D numerical model. Soil–structure interaction (SSI) analysis.

Step 1. A 3D numerical model was developed to build liquefaction potential curves in FF conditions. In particular, the soil performed in [33] was considered. The 3D soil models consisted of a $100 \times 100 \times 20$ m mesh, performed with 8000 20-node BrickUP elements and 9163 nodes to simulate the dynamic response of solid–fluid fully coupled material [54,55]. Finite elements were defined on the wavelengths of the seismic signal and the maximum frequency above which the

spectral content of the input was considered negligible (15 Hz). The dimension of the elements was increased from the structure to the lateral boundaries that were modelled to behave in pure shear and located far away from the structures, as previously applied in [32,33]. For each BrickUP element, 20 nodes described the solid translational degrees of freedom, while the eight nodes on the corners represented the fluid pressure 4 degrees-of-freedom (DOF). For each node, DOFs 1, 2 and 3, represent solid displacement (μ), and DOF 4 describes fluid pressure (p), which was recorded using OpenSees Node Recorder [55,56] at the corresponding integration points. The soil model applied the two-phase material μ - p formulation (where μ is the displacement of the soil skeleton and p is pore pressure) and simulated with PressureDependMultiYield02 (PDMY02) model [55,56], based on the multi-yield-surface plasticity framework and calibrated with centrifuge tests and consolidated undrained cyclic triaxial tests (VELACS No. 40–58), more details in [32,33]. Table 3 shows the adopted parameters, such as the low-strain shear modulus and friction angle, as well as parameters to control the contraction (c_1), dilatancy (d_1 and d_2) and the level of liquefaction-induced yield strain (l_1 , l_2 and l_3), [55,56]. The backbone curve is shown in Figure 4. The penalty method was adopted for modelling the boundary conditions (tolerance: of 10^{-4}), chosen as a compromise to be large enough to ensure strong constrain conditions but not too large to avoid problems associated with conditioning of the system of equations. Base boundaries (20 m depth) were considered rigid in all directions, and the input motions were applied at the base as acceleration time histories [32,33]. Vertical direction (described by the 3rd DOF) was constrained in correspondence with all the boundaries (at the base and lateral), while longitudinal and transversal directions were left unconstrained at lateral boundaries to allow shear deformations. The definition of the mesh dimensions followed the approach already adopted [32,33,53,54] and, to verify proper simulation of FF conditions at lateral boundaries, accelerations at the top of the meshes were compared with the FF ones, that were found to be identical, confirming the effective performance of the mesh.

Table 3. PressureDependMultiYield02 (PDMY02) model parameters.

Parameter	Value
Mass density (kN/m^3)	19.58
Reference shear modulus (Pa)	$5.8 \cdot 10^7$
Reference bulk modulus (Pa)	$7.9 \cdot 10^7$
Shear wave velocity (m/s)	170
Friction angle ($^\circ$)	30
Permeability (m/s)	10^{-8}
Peak angle ($^\circ$)	30
c_1	0.07
d_1	0.4
d_2	2
l_1	10
l_2	0.01
l_3	1

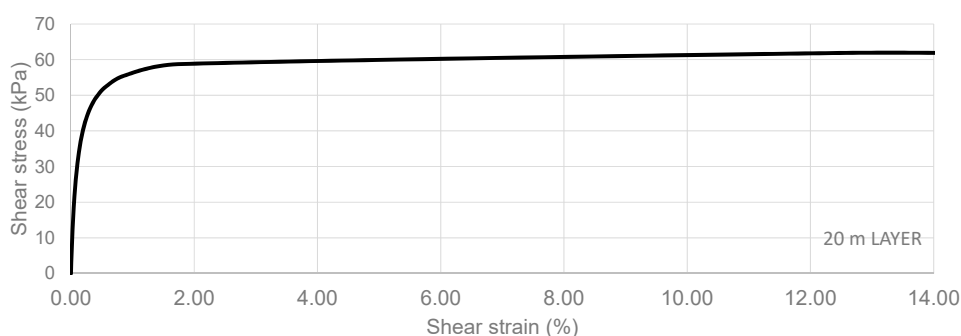


Figure 4. Backbone curve of the soil mesh.

Step 2 consisted of considering a complete system (soil + foundation + structure), Figure 3. The benchmark structure was calibrated to represent residential buildings and already applied in [33]. In this regard, a two-storey concrete structure was selected (floor height: 3.40 m, total heights: 6.80 m), with a 4×2 column scheme (4 in the longitudinal direction (8 m spaced) and 2 in the transversal direction (10 m spaced)). Some simplifications consisted of considering a shear-type behaviour (with plan and vertical regularity) and concentrating the seismic masses at each floor level. Table 4 shows the dynamic characteristics of the structure, assumed to be linear elastic and modelled with elastic-beam column elements (Table 5). A concrete shallow foundation ($28.4 \text{ m} \times 34.4 \text{ m} \times 0.50 \text{ m}$) was considered to represent recurrent typologies for residential buildings. The foundation was performed as rigid by linking all the nodes at the base of the columns together and to boundaries, by applying the equaldof [55,56]. The foundation was designed by calculating the eccentricity (the ratio between the overturning bending moment at the foundation level and the vertical forces) in the most detrimental condition of minimum vertical loads (gravity and seismic loads) and maximum bending moments. The foundation was modelled with a Pressure Independent MultiYield [55,56] as an equivalent concrete nonlinear hysteretic material with a Von Mises multi-surface kinematic plasticity model to simulate the monotonic or cyclic response of materials whose shear behaviour was insensitive to the confinement change, Table 6. The first 0.5 m of soil around the foundation was constructed of an infill layer defined by PressureDependMultiYield, and Table 7 shows the adopted parameters. The number of yield surface was equal to 20. Figure 5 shows the Backbone curve.

Table 4. Structural characteristics.

Structural Parameters	Value
n floor	2
H (m)	6.80
H/B	0.92
Bearing Pressure (kPa)	135
T_{1x} (s)	0.341 (91.77%)
T_{1y} (s)	0.331 (86.67%)
T_{2x} (s)	-
T_{2y} (s)	0.224 (3.48%)
T_{1x} (s)	0.341 (91.77%)
T_{1y} (s)	0.331 (86.67%)

Table 5. Material parameters (structure).

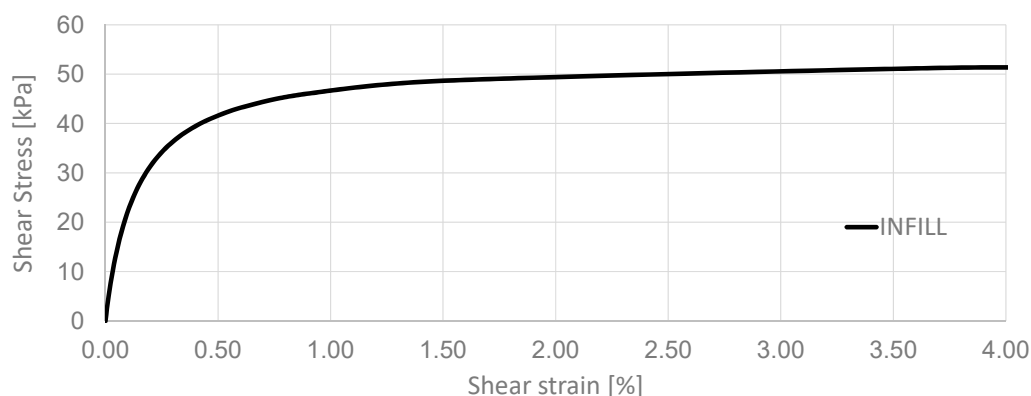
Material Parameters	Value
Young modulus (kN/ m ²)	$3.5 \cdot 10^7$
Shear modulus (kN/ m ²)	$1.73 \cdot 10^7$
Cross section area (m ²)	0.12
Inertial moment (m ⁴)	$9 \cdot 10^{-4}$

Table 6. Material parameters (foundation).

Material Parameters	Value
Mass density (kN/ m ³)	24
Reference shear modulus (kPa)	$1.25 \cdot 10^7$
Reference bulk modulus (kPa)	$1.67 \cdot 10^7$

Table 7. Material parameters (infill soil).

Material Parameters	Value
Mass density (kN/ m ³)	17.00
Reference shear modulus (Pa)	3.83·10 ⁷
Reference bulk modulus (Pa)	1.50·10 ⁷
Shear wave velocity (m/s)	150
Friction angle (°)	5
Permeability (m/s)	10 ⁻⁷

**Figure 5.** Backbone curve of the infill soil.

It is worth noting that due to the large amount of nonlinear dynamic analyses, the following simplifications were introduced to improve the computation speed: (1) The foundations were modelled as rigid slabs. (2) Deformations inside the foundation, weak soil, and intermediate nodes along the height of the superstructure were calculated during the analyses but not saved and memorised as results. (3) Concrete material was modelled as equivalent linear elastic. (4) The structure was modelled as a shear-type building by introducing rigid diaphragms. (5) The soil was modelled as an equivalent one-layered with constant shear wave velocity and (6) the base of the mesh was considered fixed (with no absorbing boundaries). These assumptions allowed the maintenance of the computation of response for the performed earthquake records in less than 72 h by using the parallel computation procedure.

4. Liquefaction-Potential Curves for Free-Field

In this section, step 1 (FF conditions) is considered. 3D nonlinear dynamic analyses (total 70) were performed, and the maximum longitudinal displacements (named lateral spread, LS) and vertical displacements (named settlements, ST) were calculated for each. Figure 6 shows the results for input motion 2 (100%). For each analysis, the LS and ST at the surface in correspondence with the centre of the mesh were considered at with liquefaction condition ($r_u = 1$) and defined on scaled PGA values (Figures 7 and 8) to evaluate the variation of demand and capacity with ground motion characteristics. In particular, standard deviation (β) defines the dispersion about the mean value, and it significantly affects the slope of the curves. In particular, higher values of β increase the probabilities at low IMs and, at the same time, they decrease the probability at high IMs. The mean value (μ) defines the central tendency of the curves affecting the translation of them inside the range of values. Thus, bigger values of the mean correspond to a higher probability of reaching or exceeding a particular damage state. In particular, Table 8 shows the comparison between the values of β and μ that affect the difference between the two liquefaction-potential (LP) curves. LP probabilities at low PGA were bigger in correspondence with ST-FF ($\beta = 0.624$) than with LS-FF ($\beta = 0.595$). The mean values (μ) also were significantly different. Figure 9 shows the LP (liquefaction potential) curves for both the

considered parameters (LS and ST), showing that both the curves represented a severe increase in the LP at a low value of PGA (low intensities). Comparing the two curves, it is worth noting that when lateral spread was considered, there was a significant difference of LP in the range of PGA = 0.20–0.30 g. For example, given an input PGA = 0.26 g, LP = 0.575 and 0.284 (around 50%), respectively, for ST-FF and LS-FF. If other levels of PGA were considered, this difference decreased significantly (at least to zero). In particular, the difference decreased gradually as the severity of the motion increased until around 0.80–0.90 g, where the curves were almost equivalent. For PGA values less than 0.20 g, referring to settlement was still more conservative than considering lateral spread. The reason for the difference is due to the fact that settlements are more sensitive to inertial forces connected with the vertical stresses (especially the weight) and start at a low value of PGA, while lateral spread needs a higher level of intensity to occur since they are connected with shear mechanisms.

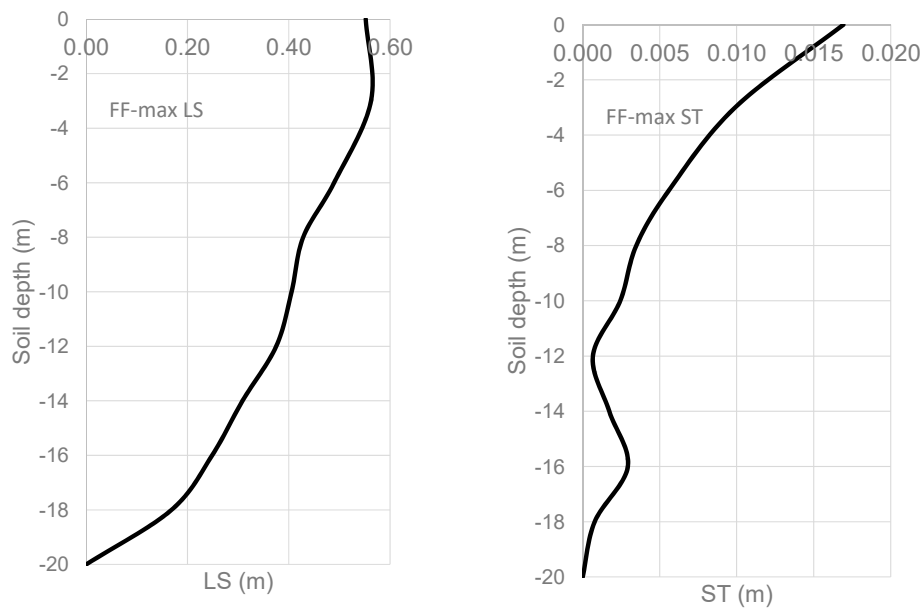


Figure 6. Free field (F: maximum lateral spread (LS) and settlement (ST) vs. soil depth (input motion 2, 100%).

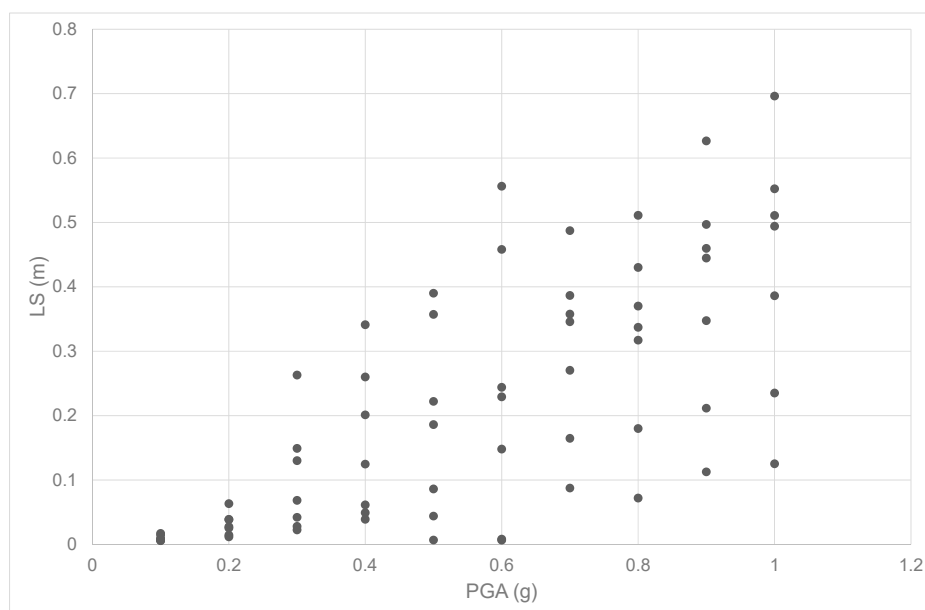


Figure 7. FF: relationships between PGA (g) and LS (m).

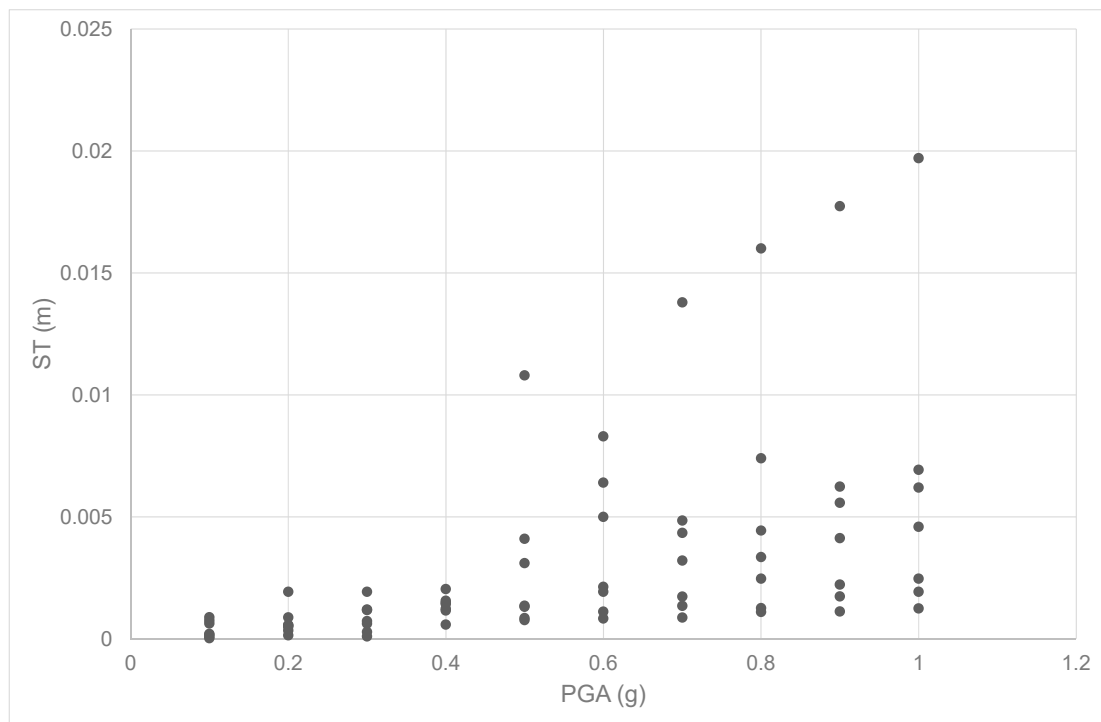


Figure 8. FF: relationships between PGA (g) and ST (m).

Table 8. Free field (FF): lognormal parameters.

Parameter	μ	B
Lateral spread	0.382g	0.595
Settlement	0.214g	0.624

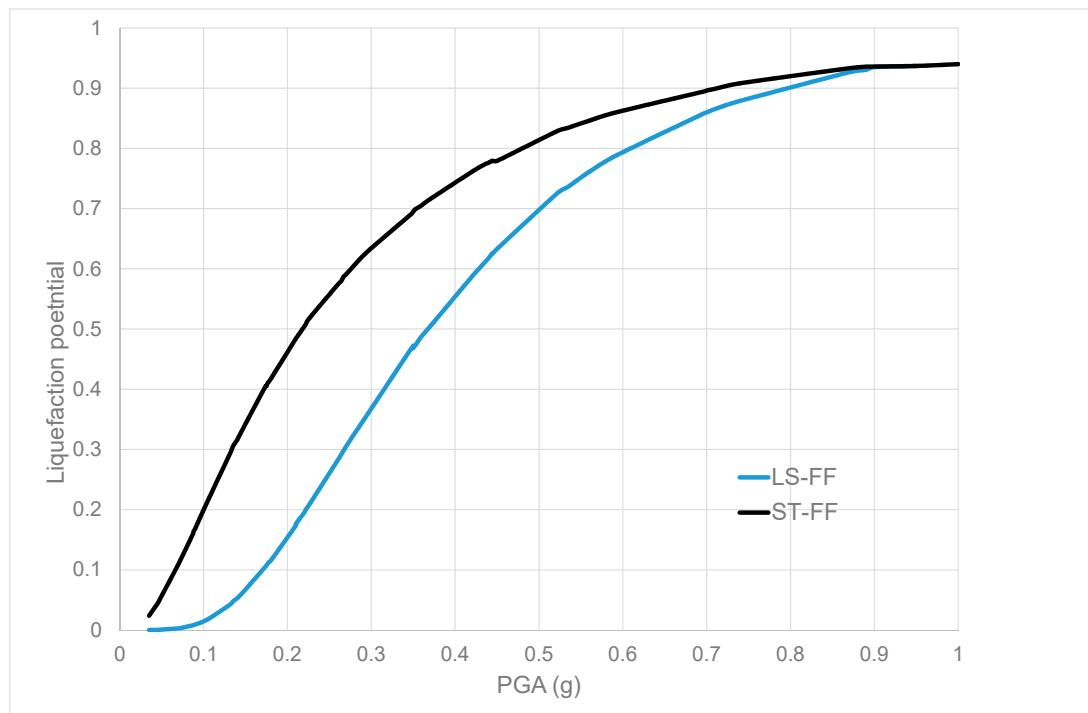


Figure 9. FF: liquefaction potential (LP): lateral spread (LS) and settlement (ST) comparison.

5. LP Curves for SSI

Step 2 is shown in this section, and the role of the structure is discussed by calculating LS and ST for the 70 3D nonlinear dynamic analyses. Figure 10 shows the results for input motion 2 (100%) to give an example of the soil behaviour. LS and ST were calculated at the surface in correspondence with the centre of the foundation that was demonstrated (see [47]) being mostly affected by the presence of the structure (mainly in terms of vertical stresses). LS and ST were considered in correspondence with liquefaction condition ($r_u = 1$) and plotted in Figures 11 and 12. Table 9 shows the comparison between the values of β and μ that affects the difference between the two LP curves. In particular, LP probabilities at low PGA were significantly bigger in correspondence with ST-SSI ($\beta = 0.653$) than with LS-SSI ($\beta = 0.624$). The mean values (μ) were significantly different. Figure 13 displays LP curves for both the considered parameters (LS and ST) showing that ST-SSI curve represented a severe increase in the LP at a low value of PGA (for earthquakes with low intensity). Comparing these two curves, it is worth noting that when lateral spread was considered, there was a significant difference of LP in the range of PGA = 0.10–0.25 g. For example, given an input PGA = 0.175 g, LP = 0.666 and 0.195 (around 30%), respectively, for ST-SSI and LS-SSI. If other levels of PGA were considered, this difference decreased significantly (at least to zero). In particular, the difference decreased gradually as the severity of the motion increased until around 0.70–0.90, where the curves were almost equivalent. These curves show the role of the structure in aggravating the vertical stresses (due to the structural weight). In particular, the low-rise structure was selected to consider the effect of a rigid and heavy superstructure on the inertial interaction between the structure and the soil that is herein demonstrated to be significantly detrimental in increasing LP values. These results confirm that the damage is mainly governed by the rigid rotations and settlements, and liquefaction works as a natural isolation system against the transmission of inertial seismic actions on the superstructure, as shown in [19].

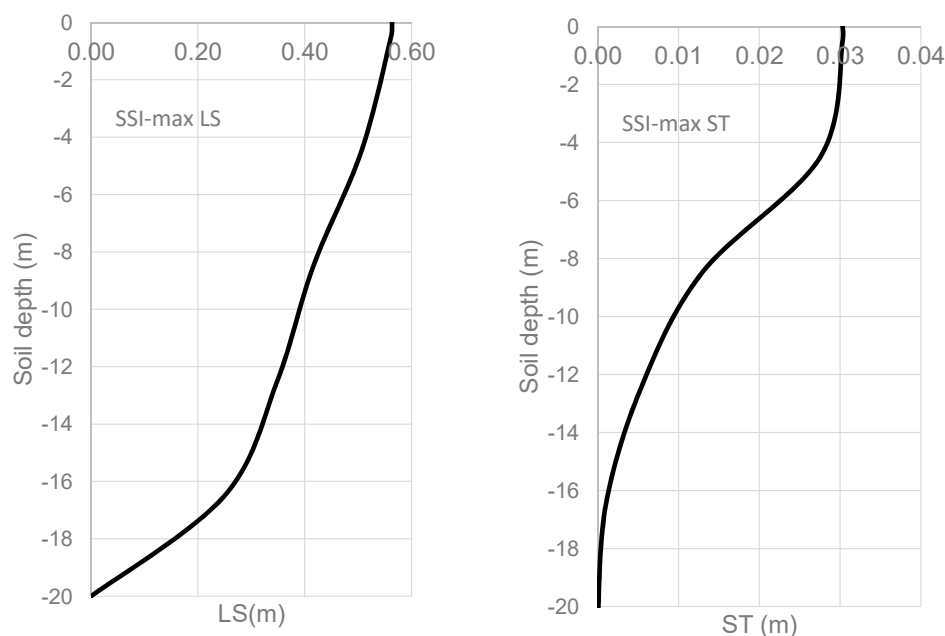


Figure 10. Soil–structure interaction (SSI): maximum lateral spread (LS) and settlement (ST) vs. soil depth (input motion 2, 100%).

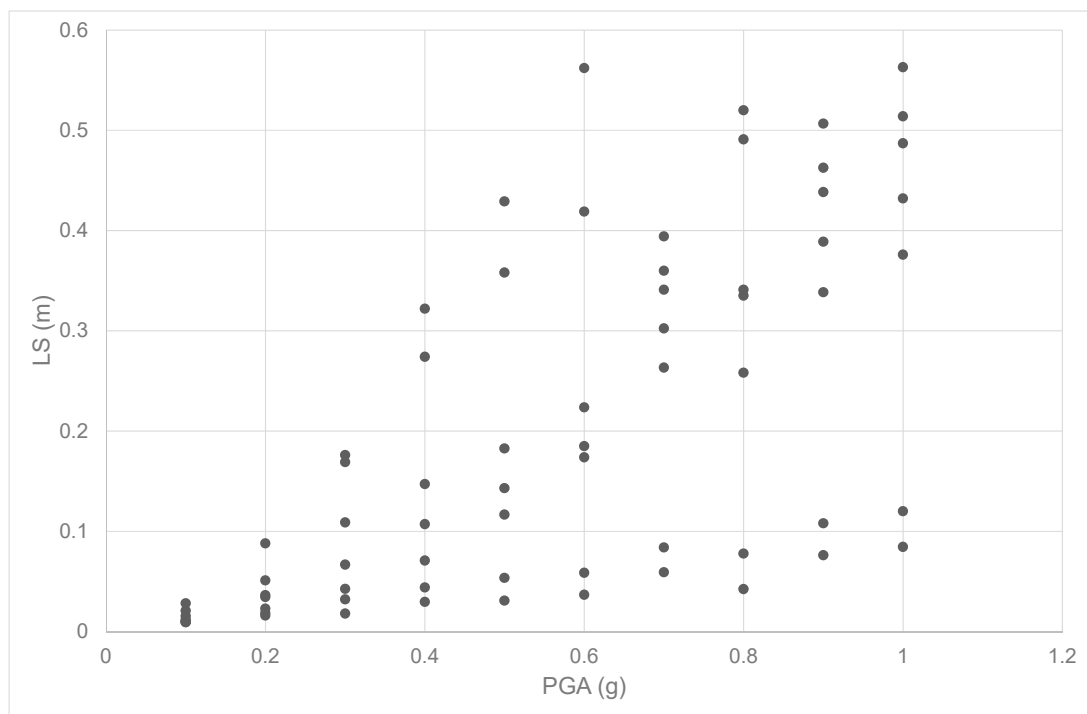


Figure 11. SSI: relationships between PGA (g) and LS (m).

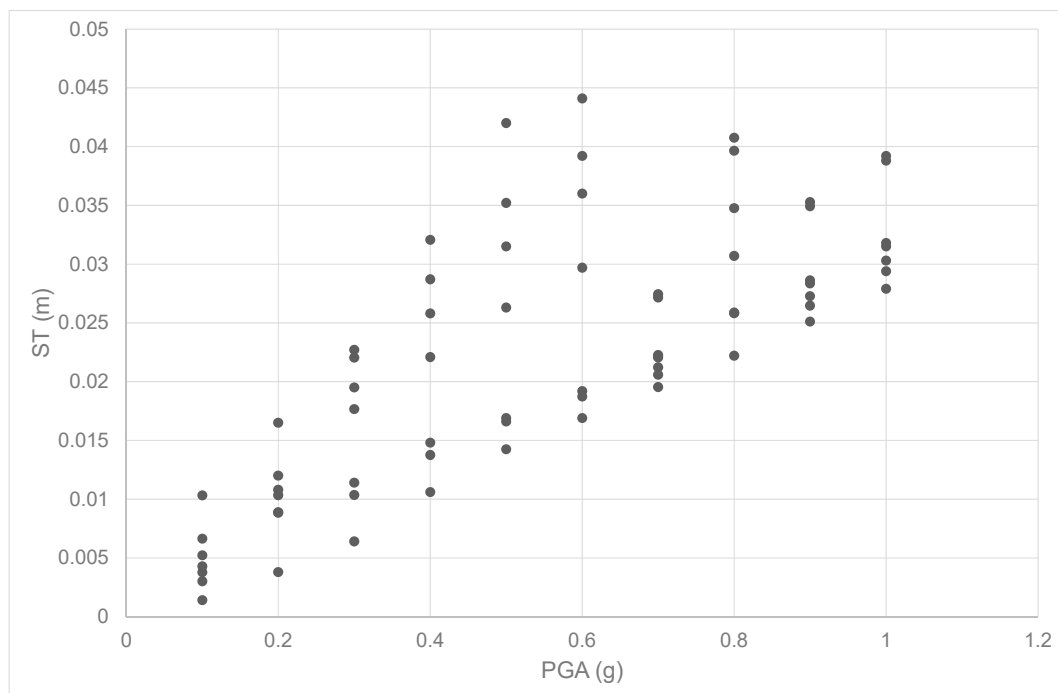


Figure 12. SSI: relationships between PGA (g) and ST (m).

Table 9. Soil–structure interaction (SSI): lognormal parameters.

Parameter	μ	β
Lateral spread	0.317g	0.624
Settlement	0.099g	0.653

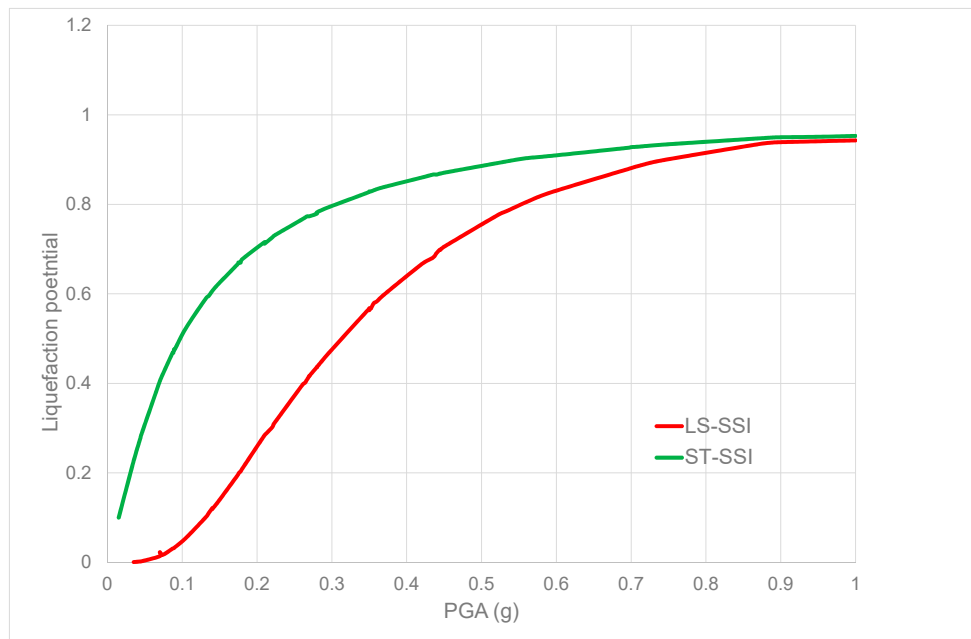


Figure 13. SSI: liquefaction potential (LP): lateral spread (LS) and settlement (ST) comparison.

The comparison between FF and SSI cases are shown in Figures 14 and 15 that plot LP curves for both the considered parameters (LS and ST). It is worth noting the detrimental effects of the presence of the structure in both cases. The role of SSI was particularly significant when the settlement was considered as a damage parameter with a severe increase in the LP values (for a range of PGA that was around 0.10–0.20 g). For example, given an input PGA = 0.148 g, LP = 0.621 and 0.337 (around 54%), respectively, for ST-SSI and ST-FF. These curves show that considering the settlement as a damage parameter is more conservative in assessing the role of the SSI.

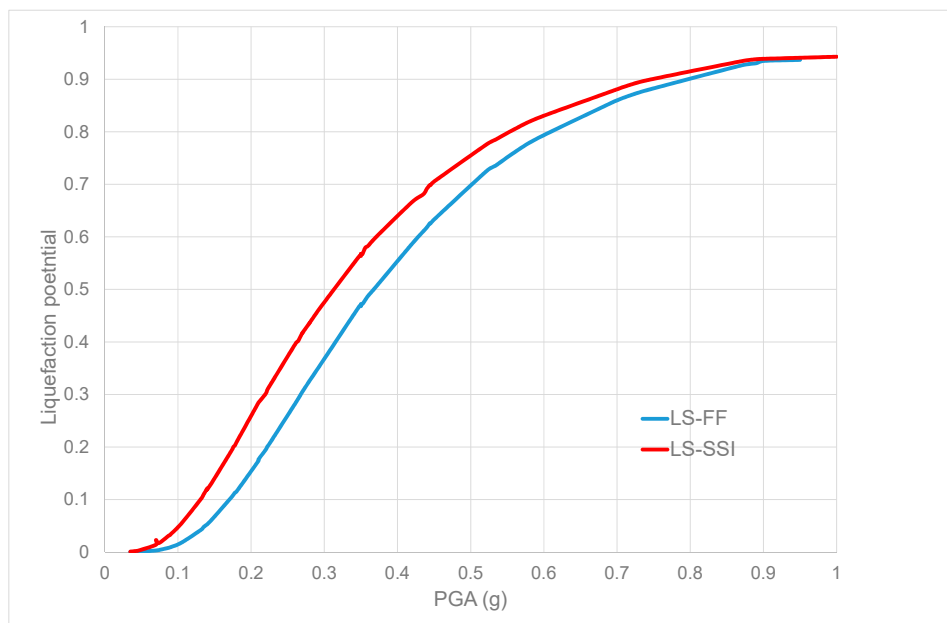


Figure 14. LS: FF-SSI LP curves comparison.

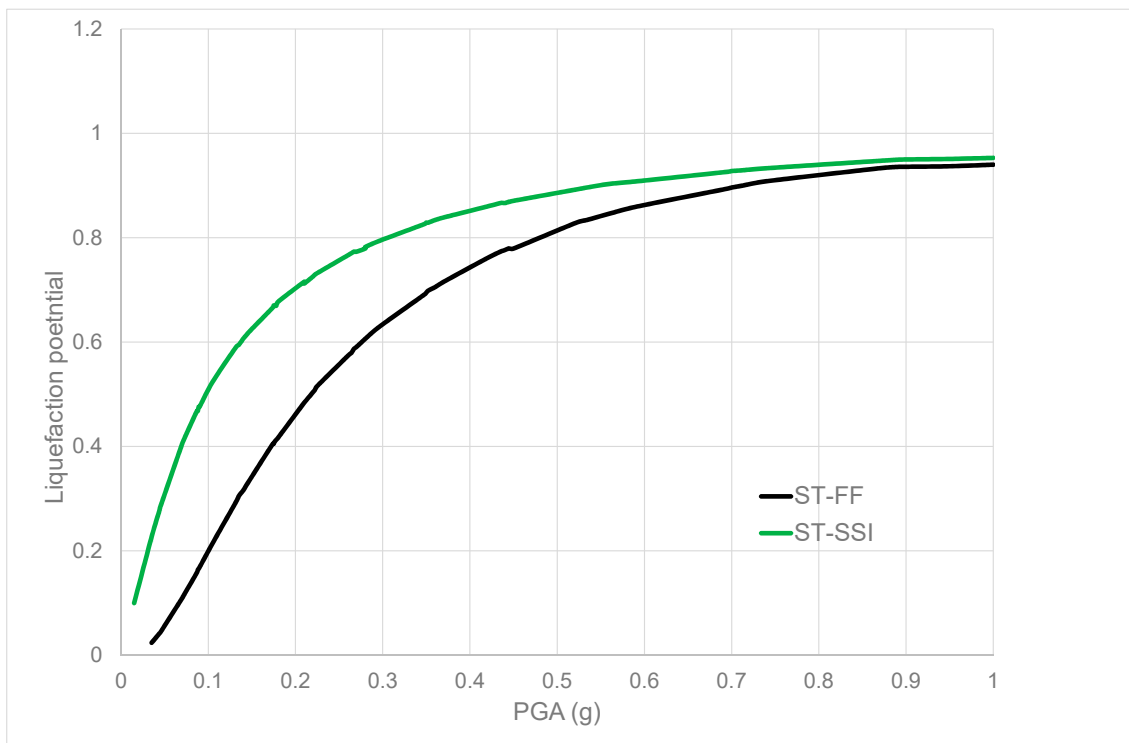


Figure 15. ST: FF-SSI LP curves comparison.

6. Conclusions

The assessment of liquefaction potential was the object of this paper. Several elements of novelty were proposed. First, a new methodology to assess liquefaction potential was described as a development of the well-established approach of fragility curves where the r_u value was applied to define liquefaction activation ($r_u = 1$). Then, the paper investigated the role of two selected parameters (the lateral spread and the settlement) by performing 140 IDA with Opensees PL in parallel computation. The findings showed that settlements are more sensitive to inertial forces connected with the vertical stresses leading to more conservative results in terms of LP (mainly for lower intensities). In addition, the role of the structure in aggravating the risk connected with liquefaction was described by two case studies performed with detailed 3D numerical models of both the soil and the structure. The findings are limited to the considered soil conditions (one-layered, with constant shear wave velocity) and numerical model assumptions (fixed base with no absorbing boundaries). In addition, the proposed analytical fragility curves need to be compared with the ones developed from the empirical database to have a full understanding of the mechanisms at the base of SSI during liquefaction events. Both of these aspects will be the object of future work.

Author Contributions: Conceptualisation, D.F.; methodology, D.F.; software, D.F.; validation, D.F.; formal analysis, D.F.; investigation, D.F.; resources, D.F.; data curation, D.F.; writing—original draft preparation, D.F.; writing—review and editing, D.F.; visualisation, D.F.; supervision, D.F.; project administration, D.F.; funding acquisition, D.F. All authors have read and agreed to the published version of the manuscript.

Funding: This research received no external funding.

Conflicts of Interest: The authors declare no conflict of interest.

References

1. Ishihara, K.; Yoshimine, M. Evaluation of settlements in sand deposits following liquefaction during earthquakes. *Soils Found* **1992**, *32*, 173–188. [[CrossRef](#)]
2. Tokimatsu, K.; Seed, H.B. Evaluation of settlements in sands due to earthquake shaking. *ASCE J. Geotech. Geoenviron. Eng.* **1987**, *113*, 861–878. [[CrossRef](#)]
3. Youd, T.L.; Hansen, C.M.; Bartlett, S.F. Revised multilinear regression equations for prediction of lateral spread displacement. *ASCE J. Geotech. Geoenviron. Eng.* **2002**, *28*, 1007–1017. [[CrossRef](#)]
4. Zhang, J.; Zhao, J.X. Empirical models for estimating liquefaction-induced lateral spread displacement. *Soil Dyn. Earthq. Eng.* **2005**, *25*, 439–450. [[CrossRef](#)]
5. Boulanger, R.W.; Mejia, L.H.; Idriss, I.M. Liquefaction at Moss Landing during Loma Prieta earthquake. *J. Geotech. Geoenviron. Eng.* **1997**, *123*, 453–467. [[CrossRef](#)]
6. Goh, A.T.C. Seismic liquefaction potential assessed by neural networks. *J. Geotech. Geoenviron. Eng.* **1995**, *120*, 1467–1480. [[CrossRef](#)]
7. Halder, A.; Tang, W.H. Probabilistic evaluation of liquefaction potential. *J. Geotech. Eng. ASCE* **1979**, *104*, 145–162.
8. Juang, C.H.; Fang, S.Y.; Khor, E.H. First order reliability method for probabilistic liquefaction triggering analysis using CPT. *J. Geotech. Geoenviron. Eng. ASCE* **2006**, *132*, 337–349. [[CrossRef](#)]
9. Juang, C.H.; Rosowsky, D.V.; Tang, W.H. Reliability based method for assessing liquefaction potential of soils. *J. Geotech. Geoenviron. Eng.* **1999**, *125*, 684–689. [[CrossRef](#)]
10. Karamitros, D.K.; Bouckovalas, G.D.; Chaloulos, Y.K.; Andrianopoulos, K.I. Numerical analysis of liquefaction-induced bearing capacity degradation of shallow foundations on a two-layered soil profile. *Soil Dyn. Earthq. Eng.* **2013**, *44*, 90–101. [[CrossRef](#)]
11. Liao, S.C.; Veneziano, D.; Whitman, R.V. Regression models for evaluating liquefaction probability. *J. Geotech. Eng.* **1988**, *114*, 389–411. [[CrossRef](#)]
12. Robertson, P.K.; Wride, C.E. Evaluating cyclic liquefaction potential using the cone penetration test. *Can. Geotech. J.* **1998**, *35*, 442–459. [[CrossRef](#)]
13. Seed, H.B.; Idriss, I.M.; Arrango, I. Evaluation of liquefaction potential using field data. *J. Geotech. Eng.* **1983**, *109*, 458–484. [[CrossRef](#)]
14. Seed, H.B.; Idriss, I.M. Simplified procedure for evaluating soil liquefaction potential. *J. Soil Mech. Found Div. ASCE* **1971**, *97*, 1249–1273.
15. Xue, X.; Yang, X. Seismic liquefaction potential assessed by support vector machines approaches fuzzy comprehensive evaluation method. *Bull. Eng. Geol. Environ.* **2016**, *75*, 153–162. [[CrossRef](#)]
16. Crespellani, T.; Madiai, C.; Vannucchi, G. Liquefaction risk analysis during earthquakes at Nocera Scalo, Italy, Part I: Assessment of liquefaction potential using simplified procedures. *Italian Geotech. J.* **2002**, *4*, 24–25.
17. Crespellani, T.; Madiai, C. Liquefaction risk analysis during earthquakes at Nocera Scalo, Italy, Part II: Total and effective stress-strain analyses for liquefaction predictions. *Italian Geotech. J.* **2002**, *4*, 46–65.
18. Crespellani, T.; Madiai, C.; Vannucchi, G. CPT-based liquefaction hazard maps for an Italian coastal area. *Italian Geotech. J.* **2003**, *4*, 46–65.
19. Di Ludovico, M.; Chiaradonna, A.; Bilotta, E.; Flora, A.; Prota, A. Empirical damage and liquefaction fragility curves from 2012 Emilia earthquake data. *Earthq. Spectra* **2020**. [[CrossRef](#)]
20. Kafali, C.; Grigoriu, M. Seismic fragility analysis: Application to simple linear and nonlinear systems. *Earthq. Eng. Struct. Dyn.* **2007**, *36*, 1885–1900. [[CrossRef](#)]
21. Chern, S.G.; Lee, C.Y. CPT-based simplified liquefaction assessment by using fuzzy-neural network. *J. Mar. Sci. Technol.* **2009**, *17*, 326–331.
22. Farrokhzad, F.; Choobbasti, A.J.; Barari, A. Liquefaction micro-zonation of Babol city using artificial neural network. *J. King. Saud. Univ. Sci.* **2012**, *24*, 89–100. [[CrossRef](#)]
23. Maria, J.S. Applying artificial neural networks for analysis of geotechnical problems. *Comput. Assist. Mech. Eng. Sci.* **2011**, *18*, 231–241.
24. Mert, T. A comparative study on computer aided liquefaction analysis methods. *Int. J. Hous. Sci.* **2013**, *37*, 121–135.
25. Samui, P.; Sitharam, T.G. Machine learning modelling for prediction soil liquefaction susceptibility. *Nat. Hazards Earth Syst. Sci.* **2011**, *11*, 1–9. [[CrossRef](#)]

26. Xue, X.H.; Yang, X.G. Application of the adaptive neuro-fuzzy inference system for prediction of soil liquefaction. *Nat. Hazards* **2013**, *67*, 901–917. [[CrossRef](#)]
27. Bray, J.; Dashti, S. Liquefaction-induced building movements. *Bull. Earthq. Eng.* **2014**, *12*, 1129–1156. [[CrossRef](#)]
28. Dashti, S.; Bray, J.D.; Pestana, J.M.; Riemer, M.; Wilson, D. Mechanisms of Seismically Induced Settlement of Buildings with Shallow Foundations on Liquefiable Soil. *J. Geotech. Geoenviron. Eng.* **2010**, *136*, 151–164. [[CrossRef](#)]
29. Dashti, S.; Bray, J.D. Numerical Simulation of Building Response on Liquefiable Sand. *J. Geotech. Geoenviron. Eng.* **2013**, *139*, 1235–1249. [[CrossRef](#)]
30. Elgamal, A.; Lu, J.; Yang, Z. Liquefaction-induced settlement of shallow foundations and remediation: 3D numerical simulation. *J. Earthq. Eng.* **2005**, *9*, 17–45. [[CrossRef](#)]
31. Elgamal, A.; Lu, J.; Forcellini, D. Mitigation of Liquefaction-Induced lateral deformation in sloping stratum: Three-dimensional Numerical Simulation. *J. Geotech. Geoenviron. Eng.* **2009**, *135*, 1672–1682. [[CrossRef](#)]
32. Forcellini, D. Numerical simulations of liquefaction on an ordinary building during Italian (20 May 2012) earthquake. *Bulletin Earthq. Eng.* **2019**. [[CrossRef](#)]
33. Forcellini, D. Soil-structure interaction analyses of shallow-founded structures on potential-liquefiable soil deposit. *Soil Dyn. Earthq. Eng.* **2020**, *133*, 106108. [[CrossRef](#)]
34. Lopez-Caballero, F.L.; Farahmand-Razavi, A.M. Numerical simulation of mitigation of liquefaction seismic risk by preloading and its effects on the performance of structures. *Soil Dyn. Earthq. Eng.* **2013**, *49*, 27–38. [[CrossRef](#)]
35. Lopez-Caballero, F.L.; Farahmand-Razavi, A.M. Numerical simulation of liquefaction effects on seismic SSI. *Soil Dyn. Earthq. Eng.* **2008**, *28*, 85–98. [[CrossRef](#)]
36. Luque, R.; Bray, J.D. Dynamic analysis of a shallow-founded building in Christchurch during the Canterbury Earthquake sequence. In Proceedings of the 6th International Conference on Earthquake Geotechnical Engineering (ICEGE), Christchurch, New Zealand, 2–4 November 2015.
37. Tonni, L.; Forcellini, D.; Osti, C.; Gottardi, G. *Modelling Liquefaction Phenomena during the May 2012 Emilia-Romagna (Italy) Earthquake*; ECSMGE: Edinburgh, UK, 2015; Volume 16, ISBN 978-0-7277-6067-8.
38. Xue, X.; Yang, X. Seismic liquefaction potential assessed by fuzzy comprehensive evaluation method. *Nat. Hazards* **2014**, *71*, 2101–2112. [[CrossRef](#)]
39. HAZUS-MH MR3. In *Multi-hazard Loss Estimation Methodology, Technical Manual*; Federal Emergency Management Agency: Washington, DC, USA, 2003.
40. Sáez, E.; Lopez-Caballero, F.; Modaresi-Farahmand-Razavi, A. Effects of the inelastic dynamic soil-structure interaction on the seismic vulnerability. *Struct. Saf.* **2013**, *33*, 51–63. [[CrossRef](#)]
41. Caverzan, A.; Solomos, G. *Review on Resilience in Literature and Standards for Critical Built-Infrastructure*; EC JRC: Luxembourg, 2014.
42. Chie, N.; Clementi, F.; Formisano, A.; Lenci, S. Comparative fragility methods for seismic assessment of masonry buildings located in Muccia (Italy). *J. Build. Eng.* **2019**, *25*. [[CrossRef](#)]
43. FEMA. *HAZUS-MH MR5: Technical Manual*; FEMA: Washington, DC, USA, 2008.
44. Kwon, O.-S.; Elnashai, A.S. Fragility analysis of a highway over-crossing bridge with consideration of soil-structure interactions. *Struct. Infrastruct. Eng.* **2013**, *6*, 159–178. [[CrossRef](#)]
45. Mina, D.; Forcellini, D.; Karampour, H. Analytical fragility curves for assessment of the seismic vulnerability of hp/ht unburied subsea pipelines. *Soil Dyn. Earthq. Eng.* **2020**. In Print. [[CrossRef](#)]
46. Ranjbar, P.R.; Naderpour, H. Probabilistic evaluation of seismic resilience for typical vital buildings in terms of vulnerability curves. *Structures* **2020**, *23*, 314–323. [[CrossRef](#)]
47. Liang, H.; Tu, J.; Guo, S.; Liao, J.; Li, D.; Peng, S. Seismic fragility analysis of a High Arch Dam-Foundation System based on seismic instability failure mode. *Soil Dyn. Earthq. Eng.* **2020**, *130*, 105981.
48. Shinozuka, M.; Feng, Q.; Lee, J.; Naganuma, T. Statistical analysis of fragility curves. *J. Eng. Mech. ASCE* **2000**, *126*, 1224–1231. [[CrossRef](#)]
49. Hwang, H.M.; Huo, J.R. Generation of hazard-consistent fragility curves. *Soil Dyn. Earthq. Eng.* **1994**, *13*, 334–354. [[CrossRef](#)]
50. Popescu, R.; Prévost, J.H.; Deodatis, G. 3D effects in seismic liquefaction of stochastically variable soil deposits. *Géotechnique* **2005**, *55*, 21–31. [[CrossRef](#)]
51. Ayyün, B.; Dueñas-Osorio, L.; Padgett, J.E.; DesRoches, R. Efficient Longitudinal Seismic Fragility Assessment of a Multispan Continuous Steel Bridge on Liquefiable Soils. *J. Bridge Eng.* **2011**, *16*, 93–107. [[CrossRef](#)]

52. Fotopoulou, S.; Karafagka, S.; Ptilakis, K. Vulnerability assessment of low-code reinforced concrete frame buildings subjected to liquefaction-induced differential displacements. *Soil Dyn. Earthq. Eng.* **2020**, *110*, 173–184. [[CrossRef](#)]
53. Forcellini, D. Cost Assessment of isolation technique applied to a benchmark bridge with soil structure interaction. *Bull. Earthq. Eng.* **2017**. [[CrossRef](#)]
54. Forcellini, D. Seismic Assessment of a benchmark based isolated ordinary building with soil structure interaction. *Bull. Earthq. Eng.* **2018**. [[CrossRef](#)]
55. Lu, J.; Elgamal, A.; Yang, Z. OpenSeesPL: 3D Lateral Pile-Ground Interaction, User Manual, Beta 1.0. Available online: <http://soilquake.net/openseespl/> (accessed on 15 August 2020).
56. Mazzoni, S.; McKenna, F.; Scott, M.H.; Fenves, G.L. *Open System for Earthquake Engineering Simulation, User Command-Language Manual*, OpenSees Version 2.0.; Pacific Earthquake Engineering Research Center, University of California: Berkeley, CA, USA, 2009.



© 2020 by the author. Licensee MDPI, Basel, Switzerland. This article is an open access article distributed under the terms and conditions of the Creative Commons Attribution (CC BY) license (<http://creativecommons.org/licenses/by/4.0/>).